

Enhancing gate control and mitigating short channel effects in 20-50 nm channel length single-gate amorphous oxide Thin Film Transistors

Chankeun Yoon,^{1,2} Yuchen Zhou,^{1,2} and Ananth Dodabalapur^{1,2,*}

¹ *Chandra Family Department of Electrical and Computer Engineering, The University of Texas at Austin, Austin, Texas 78712, USA*

² *Microelectronics Research Center, The University of Texas at Austin, Austin, Texas 78758, USA*

Email: ananth.dodabalapur@engr.utexas.edu

Abstract

Field-effect transistors (FETs) with single gates are adversely affected by short channel effects such as drain-induced barrier lowering (DIBL) and increases in the magnitude of sub-threshold swing as the channel length is reduced. Dual-gate and gate-all-around geometries are often employed to improve gate control in very short channel length transistors. This can introduce significant process complexity to the device fabrication compared to single-gate transistors. It is shown in this paper that substantial reductions in short channel effects are

possible in single-gate field-effect transistors with indium gallium zinc oxide semiconductor channels by modifying the design of the source and drain electrodes to possess an array of tapered tips which are designated as nanospike electrodes. 20-25 nm channel length FETs with nanospike electrodes have DIBL and other key metrics that are comparable to those in much larger (70-80 nm) channel length FETs with a conventional source/drain electrode design. These improvements stem from better gate control near the source and drain electrode tips due to the shape of these electrodes. These bottom gate FETs had a gate insulator consisting of 9 nm thick Al₂O₃ and independent Ni gates. This design approach is expected to be very helpful for a variety of semiconductor technologies being considered for back-end-of-line (BEOL) applications.

KEYWORDS: Amorphous oxide transistor, InGaZnO, short-channel-effect, Back-End-Of-Line

Introduction

In all field-effect transistors (FETs), gate control of the channel current, both below and above threshold, becomes increasingly difficult as the channel length is progressively reduced. A set of deleterious effects, known collectively as short channel effects (SCE) start to manifest, requiring a redesign of the device architecture for efficient FET operation. In silicon field-effect transistors, this has resulted in the predominant device architecture changing from the earlier single gate FETs (1,2) to dual gate, trigate or FINFETs (3), and eventually to gate-all-around architectures (4,5). To quantify the relationship between SCE and important FET parameters including channel length, L_{ch} , a parameter λ was introduced by Yan *et al.* (6), and is currently widely used by the research

community. The ratio L_{ch}/λ is a key metric in assessing the performance of a FET and typically needs to be more than ~ 5 for the FET to have good operating characteristics above and below threshold (7). Simple algebraic forms for λ in terms of channel parameters have been derived for single gate, double gate, as well as some more complex FET architectures (6). In general, the more extensive the electrostatic gate control of channel current, the smaller is the value of λ and hence larger L_{ch}/λ . For single gate FETs, L_{ch} is given by $\sqrt{(t_{oxide}t_{channel}\epsilon_{channel})/\epsilon_{oxide}}$, where t and ϵ are thickness and permittivity, respectively. (6,7)

It is shown in this paper that as an alternative approach to the use of double gate or more complex gate architectures, single gate FETs can be modified to result in increased L_{ch}/λ values for otherwise similar channel parameters. The essence of this approach is a specific change made to the source and drain electrode shape and configuration. As a result of such a change, it is shown that 20 nm channel length FETs with the new design have key SCE parameters such as drain induced barrier lowering (DIBL) that are comparable to those in 50-100 nm channel length FETs with a conventional electrode design that is used by most research groups. This indicates that it is possible to use single gate architectures down to much smaller channel lengths (by a factor of > 2) than is otherwise possible. This can greatly simplify the device architecture, and hence reduce fabrication complexity and cost, and will be especially useful in back-end-of-line (BEOL) circuitry comprised of amorphous oxide thin-film transistors (TFTs) (8-15). Such transistors are being actively considered for memories including dynamic random-access (16-19), artificial intelligence accelerators (20), neuromorphic circuits (21), etc. A BEOL TFT technology that is powerful and can be scaled down to very small channel lengths will be useful for designing new types of artificial intelligence (AI) hardware in conjunction with front-end silicon circuitry (22).

The main idea that is demonstrated in this paper is that a source-drain electrode geometry that has spike shaped tips (referred to as nanopikes), as illustrated in **Fig. 1**, results in substantial improvement of key FET parameters such as DIBL and sub-threshold swing (SS). This electrode design is illustrated in **Fig. 1** along with the conventional or flat-edge electrode design that is typically used by most groups. This architecture only requires a modification of the source-drain pattern and does not add any process steps or new materials to the device design. The advantages as well as trade-offs that accrue with this electrode design are discussed in a later section of the paper. In earlier publications, some quantitative aspects of this design were described for larger channel length TFTs with unpatterned gates and much thicker (90 nm) SiO₂ gate insulators (23-25). In this paper, the channel lengths are scaled down to 20-50 nm and the gate insulator equivalent oxide thickness is scaled down to ~4.7 nm. Detailed comparisons are made with equivalent conventional single gate TFTs (illustrated schematically in **Fig. 1a**) which has 6 nm thick IGZO channel and 9 nm thick Al₂O₃ gate insulator, resulting in a λ value of 8.5 nm. A series of comparisons are made between characteristics of 20-50 nm channel length nanopike TFTs and conventional flat-edge TFTs. The active semiconductor material used is indium gallium zinc oxide (IGZO); however, the designs proposed are equally applicable for other oxide semiconductors based TFTs and indeed, single gate FETs with a variety of emerging semiconductors (26-29) and gate insulator materials (30). FETs with the new design can be conveniently combined in the same circuit with conventional FETs as the only changes are in electrode geometry, with all other layers being the same.

Results and Discussion

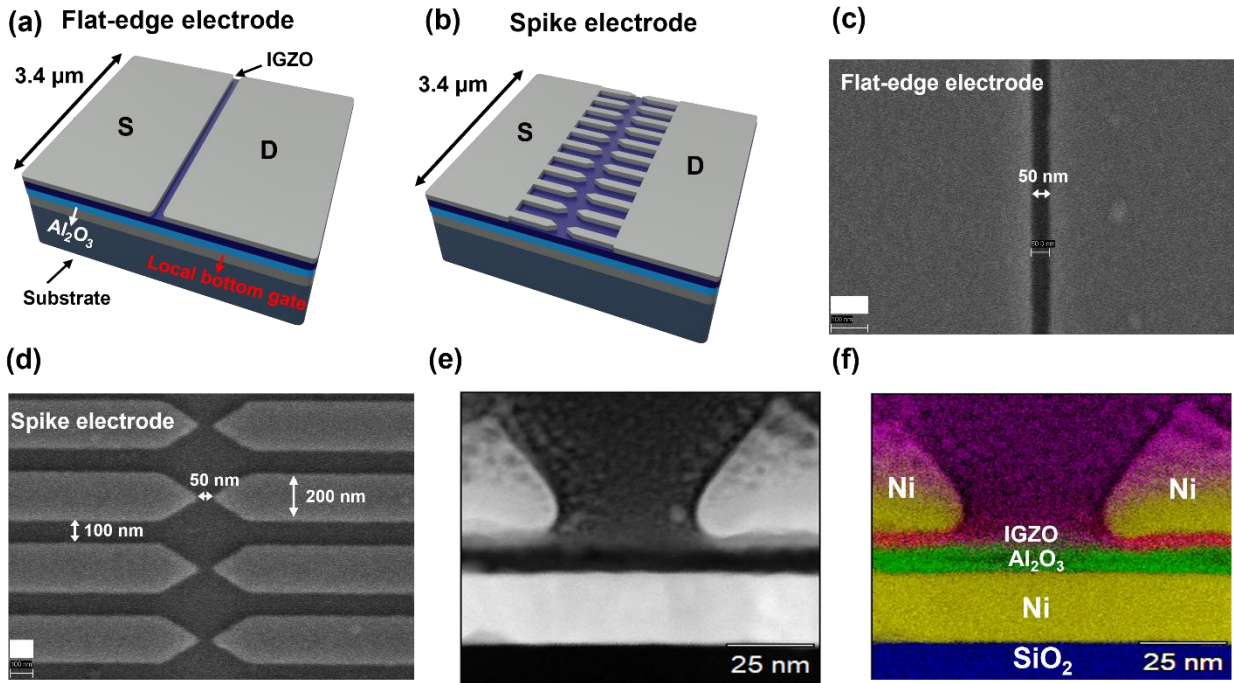


Figure 1. Schematic structures of bottom-gate, top-contact a-IGZO TFTs with (a) conventional flat-edge and (b) spike shaped source/drain electrodes. Top-view scanning electron microscopy (SEM) images of 50 nm L_{ch} devices with (c) flat-edge and (d) spike electrodes. (scale bar: 100 nm) (e) Cross-sectional Transmission Electron Microscopy (TEM) image with (f) energy dispersive X-ray spectroscopy (EDS) elemental mapping of the 50 nm L_{ch} flat-edge device.

Figure 1a and **1b** illustrate schematic structures of the a-IGZO TFTs with conventional flat-edge and spike-shape electrodes, respectively. The nanopike configuration proposed in this work consists of an array of spike-shaped electrodes with gaps in between, as illustrated in **Fig. 1b**. Detailed device fabrication steps are provided in the Methods section. As shown in **Fig. 1d**, each spike electrode consists of 200 nm wide metal electrode separated by 100 nm gap between adjacent electrodes. The impact of spike-to-spike spacing on device performance at both 1000 nm and 50 nm L_{ch} are further illustrated in **Fig. S1**. **Figure. 1e** and **1f** show cross-sectional TEM images of

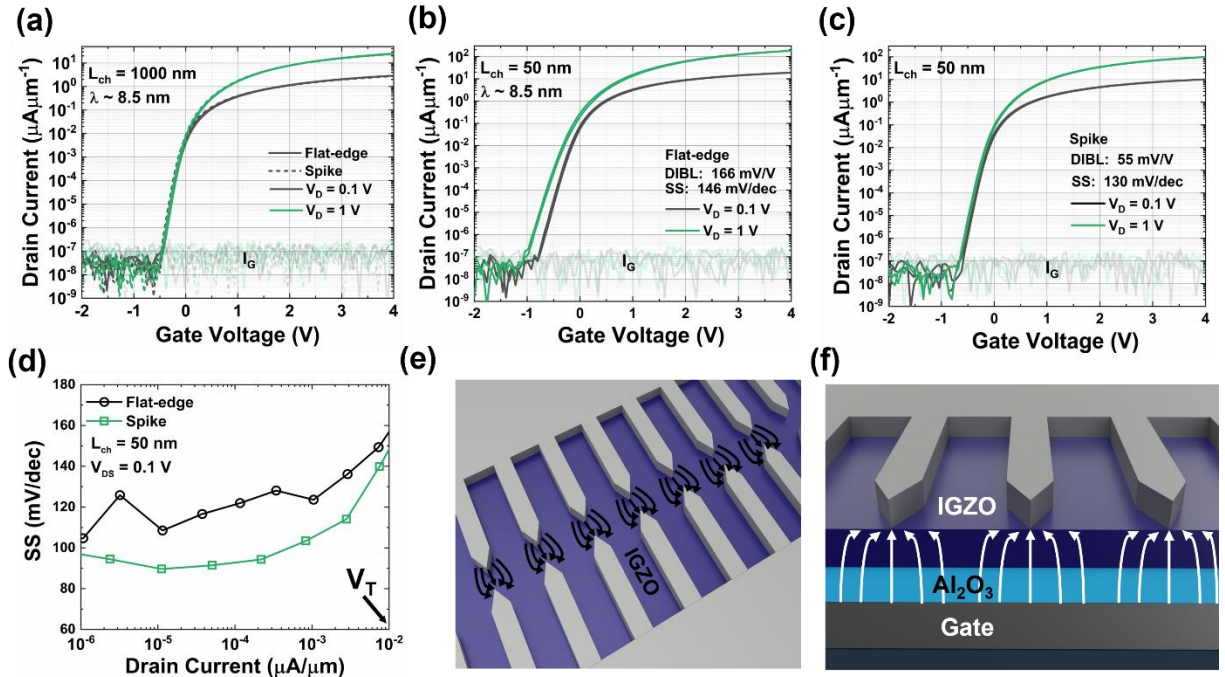


Figure 2. I_D - V_G transfer characteristics of (a) spike and flat-edge device with $L_{ch} = 1000$ nm and (b) a flat-edge device and (c) a spike device with $L_{ch} = 50$ nm. The spike devices have significantly lower DIBL as well as lower SS compared to the conventional flat-edge electrode devices with same L_{ch} (d) SS vs I_D of 50 nm L_{ch} devices during forward sweep near V_T regime. Schematic illustration of (e) lateral and (f) vertical electric field distributions in the spike device.

representative 50 nm L_{ch} flat-edge device with 9 nm thick Al_2O_3 and 6 nm thick IGZO. The EDS mapping images of each element are shown in Fig. S2.

A comparison between the characteristics of spike FETs and those of conventional flat-edge electrode FETs are illustrated in Fig. 2 and Fig. 3. Figure 2 illustrates the I_{DS} vs V_{GS} of devices with spike and flat-edge electrode at $L_{ch} = 1000$ nm and 50 nm, highlighting the effect of the nanospike structure in mitigating SCEs. All drain current values are normalized by the channel width (3.4 μm) for both flat-edge and spike devices. For nanospike FETs, the channel width includes the spaces between individual nanospikes. Electrical measurements are performed under both forward/reverse voltage sweep, with negligible hysteresis and small gate leakage currents. The threshold voltage, V_T is defined as a gate voltage at which drain current reaches $10 \text{ nA}/\mu\text{m}^{-1}$

and λ is estimated to be ~ 8.5 nm, using a relative dielectric constant of ~ 10 for IGZO (31). This method, or a closely related method, of defining V_T is often used by researchers for convenience (10,32). At 1000 nm L_{ch} (i.e., $L_{ch}/\lambda \sim 117$), both devices exhibit negligible DIBL, implying strong gate control over channel (**Fig. 2a**). Also, the spike and flat-edge device show comparable I_{DS} . This is illustrated in additional detail in **Fig. S3a**. As L_{ch} is reduced to 50 nm ($L_{ch}/\lambda \sim 5.88$), flat-edge electrode FETs exhibit significant SCE with increased DIBL of 166 mV/V and SS of 146 mV/dec (**Fig. 2b**). In contrast, the spike device maintains a low DIBL of 55 mV/V and SS of 130 mV/dec, indicating improved immunity to SCEs (**Fig. 2c**). **Figure 2d** compares SS vs I_{DS} , demonstrating the effectiveness of spike geometry in reducing SS compared to flat-edge electrode FETs. At L_{ch} of 50 nm, the spike device exhibits slightly lower I_{DS} compared to the flat-edge electrode FET. This is likely result of a combination of several effects including: i) a noticeable negative V_T shift in the flat edge FET due to severe DIBL; ii) a smaller effective channel width in the spike device due to the spaces between the individual spikes not contributing fully to channel current; iii) a reduced effective carrier velocity in the spike structure due to lower average electric fields in the channel (33); and (iv) higher DIBL in the flat-edge electrode FETs resulting in higher currents due to injection and transport in the bulk of the semiconductor (which is 6 nm thick), away from the interface. The lower effective electric field in the channel in the spike FET, for the same channel length and operating voltages, is a result of a higher field near the electrode tips shown in simulations (33). However, the electrostatic improvement of the spike device can be attributed to its electric field distribution in the channel as schematically illustrated in **Fig. 2e** and **2f**. As shown in **Fig. 2e**, the nanopike electrodes enhance the lateral electric field near the spike tips, thereby also reducing the lateral average electric field in the channel (33). In contrast, the flat-edge devices have a larger average lateral electric field (and hence carrier velocity) in the channel.

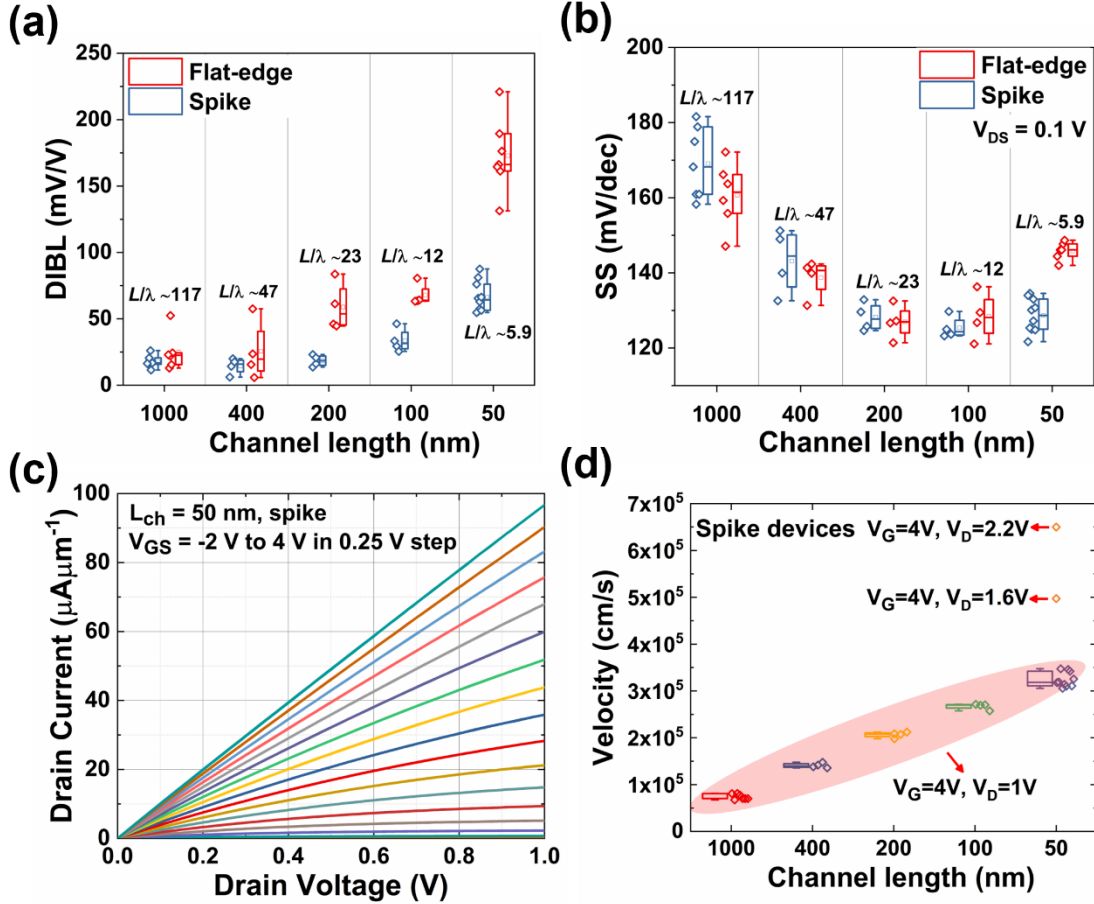


Figure 3. (a) DIBL vs L_{ch} ; also indicated are the corresponding λ values. The substantially lower DIBL values for the spike devices compared to the conventional flat-edge devices for the same channel length is clearly seen. (b) SS vs L_{ch} of flat-edge and spike devices. (c) I_D - V_D output characteristic of 50 nm L_{ch} spike device. (d) Average carrier velocity in spike devices in the linear region of operation for various channel lengths and bias conditions.

A second effect of the spike shape is enhancing gate control of channel current by a more efficient lateral control near the tips. **Figure 2f** illustrates the vertical electric field distribution in nanospike devices. Unlike flat-edge devices, the nanospike geometry results in the gate electric field concentrating near the spike tips, even in the bulk of the IGZO channel away from the semiconductor-insulator interface, which helps mitigate SCE. The spike geometry can provide several advantages besides the ones described above. In addition to providing enhanced gate control over channel that effectively suppress SCEs at small L_{ch} , the spike electrode can reduce

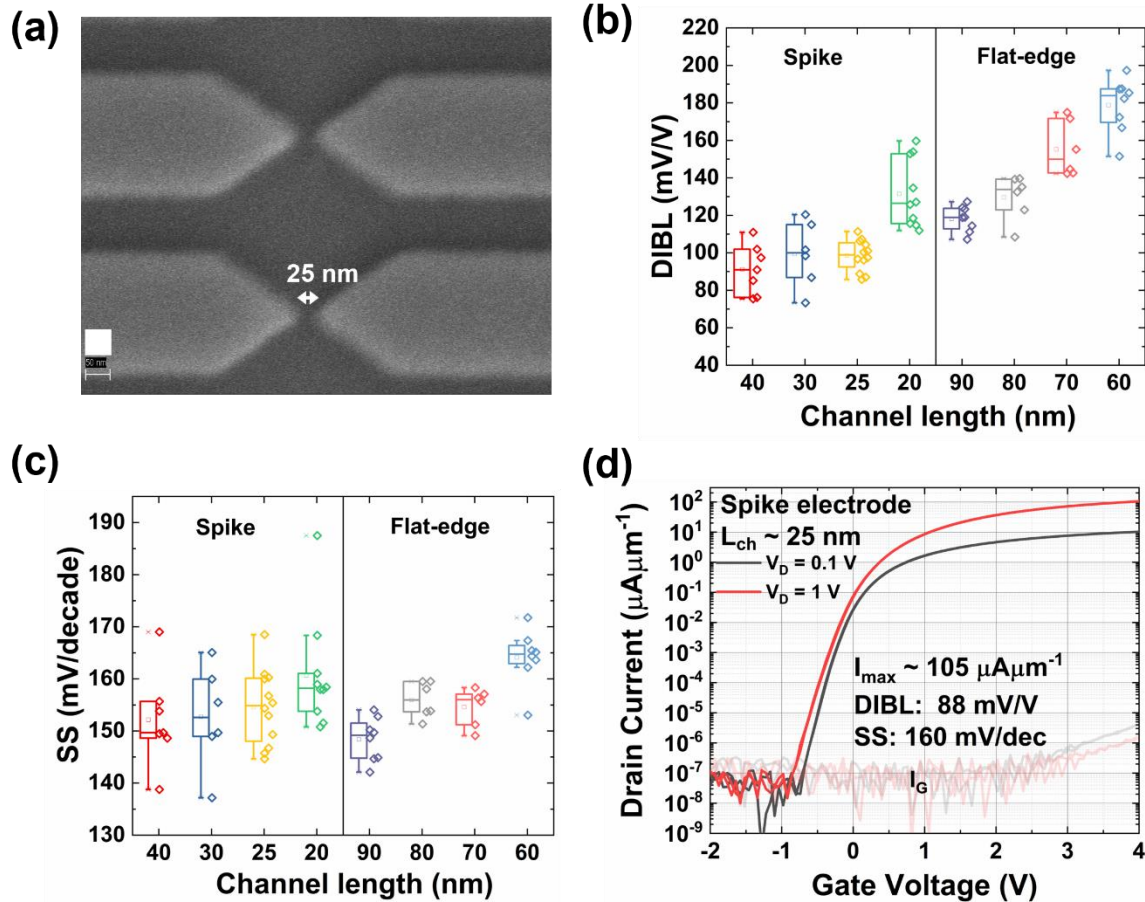


Figure 4. (a) Top view SEM image of 25 nm L_{ch} spike device. (scale bar: 50nm) (b) DIBL vs L_{ch} , (c) SS vs L_{ch} of flat-edge and spike devices. (d) I_D - V_G transfer characteristic of 25 nm L_{ch} spike device.

gate-to-source and gate-to-drain overlap areas. This reduction in overlap could lower parasitic overlap capacitance, thereby enhancing the switching speed of device. The trends in DIBL and SS as a function of channel length are illustrated in **Fig. 3a** and **3b** for nanospike and flat-edge FETs. DIBL is comparable for nanospike and flat-edge FET at larger channel lengths above 200 nm, whereas at $L_{ch} = 200$ nm and lower, DIBL values are substantially lower for nanospike geometry FETs. The SS values are comparable at channel lengths above 100 nm, and diverge significantly at 50 nm channel lengths, with the nanospike FETs maintaining a low SS value, while the flat-edge FETs have markedly higher SS values. V_T values of both devices at various L_{ch} are illustrated

in **Fig. S4**. The output characteristics (I_{DS} vs V_{DS}) of a 50 nm L_{ch} spike device is shown in **Fig. 3c**, exhibiting maximum I_{DS} of $96.7 \mu\text{A}\mu\text{m}^{-1}$ under $V_{DS} = 1\text{V}$ and $V_{GS} - V_T = 4.17\text{V}$. In **Fig. 3d**, the average carrier velocity extracted from linear-regime ($v = I_{DS} / (WC_{ox}(V_{GS} - V_T))$) is plotted as a function of L_{ch} . A peak carrier velocity of $6.5 \times 10^5\text{ cm/s}$ is achieved under $V_G = 4\text{V}$ and $V_D = 2.2\text{V}$ with superior gate control even at large drain bias, as shown in **Fig. S5**.

Performance of spike devices at channel lengths in the range 20—40 nm is illustrated in **Fig. 4**. All devices reported in **Fig. 4** were fabricated in the same batch. For comparison, flat-edge device characteristics are shown for channel lengths in the range 60-90 nm, which provide an appropriate basis to compare with nanospike FETs. The yield of flat-edge FETs with channel lengths below 50 nm was very small due to fabrication constraints. For this reason, data for flat-edge FETs with channel lengths in the range 20-40 nm could not be shown in **Fig. 4**. It is seen in **Fig. 4b** that the DIBL value of 20 nm channel length nanospike FETs is roughly comparable to that in 70–80 nm channel length flat edge FETs, providing a remarkable illustration of the utility and efficacy of the nanospike geometry FETs proposed in this work. The SS value for the 20 nm nanospike FET, shown in **Fig. 4c**, is comparable to that of much larger channel length flat-edge electrode FETs, again demonstrating the advantages of the nanospike FET vis-à-vis the conventional design. Importantly, these advantages become ever more important as the channel lengths are reduced to result L_{ch}/λ values of < 5 . In this regime, conventional single gate FETs typically possess inadequate gate control. This is evident, for example, in recent publications on single gate IGZO FETs with channel lengths below 50 nm. (18) For this technologically crucial regime of channel length, nanospike electrode FETs will allow the use of single gate geometries without compromising the device characteristics. The comparable magnitudes of SCE in 20 nm channel length nanospike FETs and ~ 70 nm flat-edge FETs underline the utility of the nanospike geometry

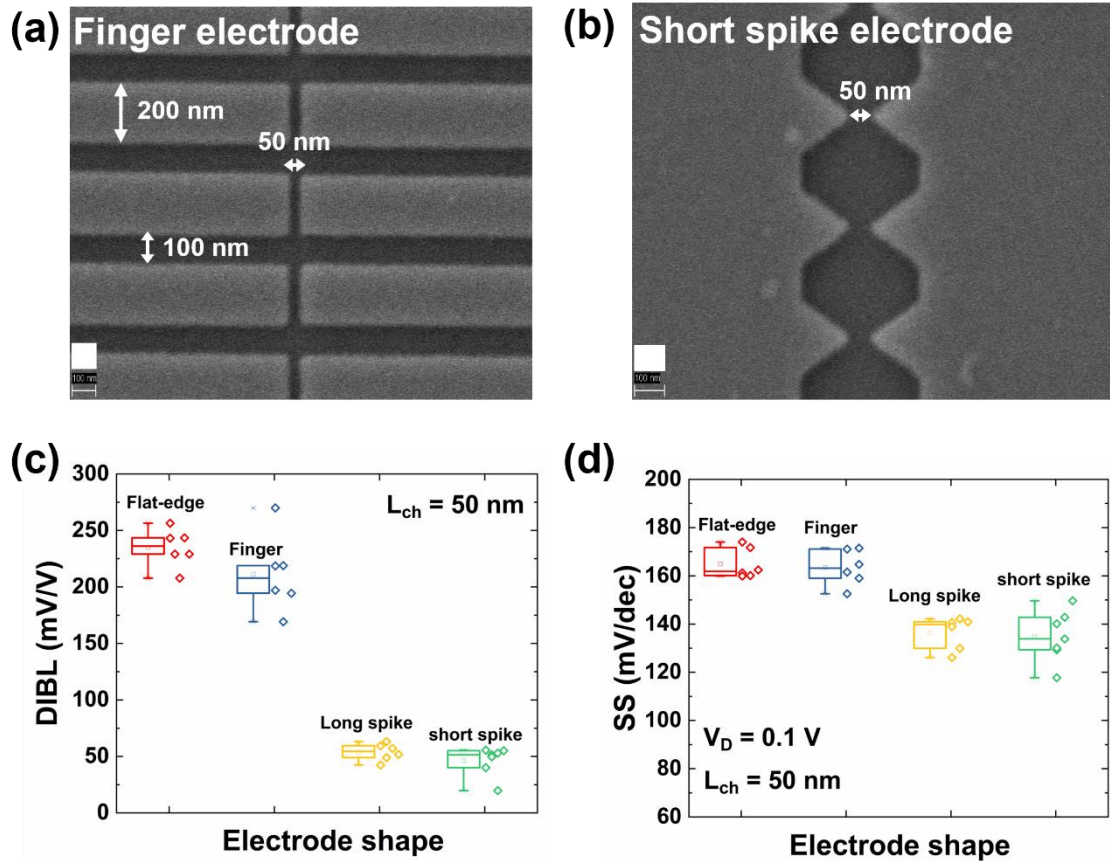


Figure 5. Top-view scanning electron microscopy (SEM) images of 50 nm L_{ch} devices with (a) finger electrode and (b) short spike electrode. (scale bar: 100 nm). (c) DIBL and (d) SS comparisons for various electrode geometries at L_{ch} of 50 nm. The SEM image of the long spike electrode device is shown in **Fig. 1(d)**

in practical applications. The transfer and output characteristics of a 25 nm L_{ch} spike device are shown in **Fig. 4d** and also in **Fig. S6**. The device achieves on-current ($\sim 105 \mu\text{A}\mu\text{m}^{-1}$) with a low DIBL (88 mV/V) and SS (160 mV/dec), confirming that the nanospike structure supports aggressive L_{ch} scaling without compromising key electrical metrics.

To understand which design features of the nanospike electrode FET are responsible for this excellent performance at smaller channel lengths, comparisons were made of characteristics of two other geometries related to that of the nanospike FETs reported in this paper. These diagnostic geometries are illustrated in **Fig. 5a** and **5b**. All devices reported in **Fig. 5** were fabricated in the

same batch, as described in the methods section below, but without encapsulation with PMMA. These diagnostic FET geometries are designated as finger electrode FETs and short spike FETs, as illustrated. The finger electrode FET has the same ratio of electrode spacing to electrode width that the nanopike FETs reported above possess. The only difference is that the electrode tips are flat-edged instead of tapered. The short spike geometry is similar to the earlier nanopike FETs except that the spike region is less elongated and more compact and hence takes up less area, which is important for increasing the density of FETs that can be fabricated in a given area. As summarized in **Figs. 5c** and **5d**, both long and short spike configurations exhibit lower DIBL and SS compared to flat-edge and finger electrode devices at $L_{ch} = 50$ nm. Notably, the short spike devices show suppressed SCEs which are comparable to the long-spike devices. In contrast, the finger-shaped electrodes, despite having an increased effective channel length due to the central gap, exhibit pronounced SCEs, with DIBL and SS values similar to those of flat-edge electrode devices. (**Fig. S7**) This indicates that the spacing between electrodes, which finger electrode FETs have in common with nanopike FETs, is in itself insufficient to suppress SCEs, thereby highlighting the importance of electrostatic control provided by the tapered end of the spike geometry devices (both short spike and long spike). The similarity between the characteristics of the short spike and long spike FETs show that the tapering is the crucial aspect of the design that provides better gate control and reduced SCE. This tapered geometry is crucial for better gate control of drain current and especially at small channel lengths. The data shows that with the use of nanopike electrodes, the simpler single-gate geometry can be used down to smaller channel lengths than is possible with conventional FET geometries, obviating the need for multiple gate and three-dimensional geometries. This advantage can be very useful in designing dense, multi-level, BEOL FET circuitry for future applications.

Conclusion

This study demonstrates that nanopike electrodes can improve SCEs in a-IGZO TFTs compared to conventional flat-edge electrodes. By comparing DIBL and SS across various L_{ch} and electrode geometries, it is established that the nanopike electrode geometry results in characteristic length (λ) reduction, which is beneficial for scaling down the L_{ch} of transistors without compromising performance. The DIBL in a 20-25 nm channel length nanopike electrode FETs is comparable to that in a much larger channel length (70-80 nm) conventional FETs that are fabricated alongside. These findings highlight the nanopike geometry as a promising structural approach for device scaling and BEOL compatible amorphous oxide TFTs. Moreover, the design concept is likely also benefit a wide range of emerging semiconductor-based short L_{ch} TFTs and can be extended to multi-gate topologies as well.

Methods

Device Fabrication

First, an 86 nm SiO₂ layer is thermally grown on p⁺⁺ Si substrates. The 25 nm nickel (Ni) local bottom gate electrode is defined using electron beam lithography (JBX-8100FS/E) and electron beam evaporation system (PRO Line PVD 200). Following this, a 9 nm Al₂O₃ gate insulator layer is deposited via atomic layer deposition at 200 °C (Fiji F200). A 6 nm thick IGZO channel is deposited above the gate insulator by RF-sputtering at 150 W at 5 mTorr with 7% O₂ pressure (PVD75). The IGZO deposition is done at room temperature with a base pressure of $\sim 2.5 \times 10^{-3}$ Torr. After deposition, the devices are annealed on a hotplate at 350 °C for 1 hour in air. Then, the IGZO channels are patterned using electron beam lithography and wet-etching using a diluted HCl etch solution. Source and drain electrodes (Ni) are patterned using the electron beam lithography

and lift-off. For source/drain formation, diluted ZEP (ZEP520A:anisole = 1:2) resist is spun at 2000 rpm for 60 s and baked at 180 °C for 2 minutes. An electron beam energy of 100 keV is used for lithography. ~30 nm Ni is deposited via electron beam evaporation system, followed by lift-off in Remover PG. Finally, PMMA A4, which serves as an encapsulation layer, is spin-coated and annealed at 180 °C for 2 minutes. Then, windows in PMMA are defined for contacting gate, source and drain electrodes. All fabrication processes are performed at temperature below 350 °C, making the entire process compatible with BEOL requirements.

Device Characterization

Electrical measurements are performed with an Agilent 4155C semiconductor parameter analyzer, at room temperature, in a dark environment and under vacuum ($\sim 6 \times 10^{-5}$ Torr).

Scanning electron microscopy

SEM images of the IGZO TFTs used in this study are obtained using a Zeiss Gemini 460 SEM system at an accelerating voltage of 5 kV.

Supporting Information

Electrical properties of spike electrode devices with various spacing between spike electrodes, cross-sectional TEM images with EDS elemental mapping, field effect mobility of device, electrical properties of Al₂O₃ capacitor, V_T of devices at various L_{ch} , I_D - V_G curve of 50 nm L_{ch} spike device at $V_D = 0.1$ V and 2.2 V, I_D - V_D curve of 25 nm L_{ch} spike device, I_D - V_G of 50 nm L_{ch} finger and short-spike device.

AUTHOR INFORMATION

Corresponding Author

Ananth Dodabalapur – Chandra Family Department of Electrical and Computer Engineering, The University of Texas at Austin, Austin, Texas 78712, USA; Microelectronics Research Center, The University of Texas at Austin, Austin, Texas 78758, United States; Email: ananth.dodabalapur@engr.utexas.edu

Authors

Chankeun Yoon – Chandra Family Department of Electrical and Computer Engineering, The University of Texas at Austin, Austin, Texas 78712, USA; Microelectronics Research Center, The University of Texas at Austin, Austin, Texas 78758, USA

Yuchen Zhou – Chandra Family Department of Electrical and Computer Engineering, The University of Texas at Austin, Austin, Texas 78712, USA; Microelectronics Research Center, The University of Texas at Austin, Austin, Texas 78758, USA

Author Contributions

C.Y. and A.D. conceived the experiments and wrote the manuscript. C.Y. fabricated devices and performed electrical characterization. Y. Z. assisted with IGZO deposition. The manuscript was written through contributions of all authors. All authors have given approval to the final version of the manuscript.

Data availability

All data are available in the paper and Supplementary Information are available from the corresponding author upon reasonable request.

ACKNOWLEDGMENT

The authors would like to thank Dr. Ioana R. Gearba-Dolocan and Dr. Xun Zhan at University of Texas at Austin (Texas Materials Institute) for TEM sample preparation and characterization. The author would like to thank Juhan Ahn at University of Texas at Austin for technical discussions.

This work was supported by the National Science Foundation under Grant No. CMMI-1938179 and by Keck foundation under grant #26753419. The work was done at the Texas Nanofabrication Facility supported by the National Science Foundation under Grant NNCI-2025227.

REFERENCES

- (1) Ghani, T.; Armstrong, M.; Auth, C.; Bost, M.; Charvat, P.; Glass, G.; Hoffmann, T.; Johnson, K.; Kenyon, C.; Klaus, J. et al., A 90nm high volume manufacturing logic technology featuring novel 45nm gate length strained silicon CMOS transistors, *IEEE International Electron Devices Meeting 2003*, IEEE: 2003; pp 11.6. 1-11.6. 3.
- (2) Mistry, K.; Allen, C.; Auth, C.; Beattie, B.; Bergstrom, D.; Bost, M.; Brazier, M.; Buehler, M.; Cappellani, A.; Chau, R. et al., A 45nm logic technology with high-k+ metal gate transistors, strained silicon, 9 Cu interconnect layers, 193nm dry patterning, and 100% Pb-free packaging, *IEEE International Electron Devices Meeting*, IEEE: 2007; pp 247-250.
- (3) Auth, C.; Allen, C.; Blattner, A.; Bergstrom, D.; Brazier, M.; Bost, M.; Buehler, M.; Chikarmane, V.; Ghani, T.; Glassman, T et al., A 22nm high performance and low-power CMOS technology featuring fully-depleted tri-gate transistors, self-aligned contacts and high density MIM capacitors, *2012 symposium on VLSI technology (VLSI)*, IEEE: 2012; pp 131-132.
- (4) Bae, G.; Bae, D.-I.; Kang, M.; Hwang, S.; Kim, S.; Seo, B.; Kwon, T.; Lee, T.; Moon, C.; Choi, Y et al., 3nm GAA technology featuring multi-bridge-channel FET for low power and high performance applications, *2018 IEEE International Electron Devices Meeting (IEDM)*, IEEE: 2018; pp 28.7. 1-28.7. 4.
- (5) Agrawal, A.; Chakraborty, W.; Li, W.; Ryu, H.; Markman, B.; Hoon, S.; Paul, R.; Huang, C.; Choi, S.; Rho, K. et al., Silicon RibbonFET CMOS at 6nm Gate Length, *2024 IEEE International Electron Devices Meeting (IEDM)*, IEEE: 2024; pp 1-4.
- (6) Yan, R.-H.; Ourmazd, A.; Lee, K. F., Scaling the Si MOSFET: From bulk to SOI to bulk. *IEEE transactions on electron devices* **1992**, *39* (7), 1704-1710.
- (7) Cao, W.; Bu, H.; Vinet, M.; Cao, M.; Takagi, S.; Hwang, S.; Ghani, T.; Banerjee, K., The future transistors. *Nature* **2023**, *620* (7974), 501-515.
- (8) Nomura, K.; Ohta, H.; Takagi, A.; Kamiya, T.; Hirano, M.; Hosono, H., Room-temperature fabrication of transparent flexible thin-film transistors using amorphous oxide semiconductors. *nature* **2004**, *432* (7016), 488-492.

- (9) Wahid, S.; Daus, A.; Kumar, A.; Wong, H.-S. P.; Pop, E. First demonstration of dual-gated indium tin oxide transistors with record drive current~ 2.3 mA/ μm at $L \approx 60$ nm and $V_{DS} = 1$ V, *2022 International Electron Devices Meeting (IEDM)*, IEEE: 2022; pp 12.5. 1-12.5. 4.
- (10) Zhang, J.; Zhang, Z.; Lin, Z.; Xu, K.; Dou, H.; Yang, B.; Zhang, X.; Wang, H.; Ye, P. D. First Demonstration of BEOL-Compatible Atomic-Layer-Deposited InGaZnO TFTs with 1.5 nm Channel Thickness and 60 nm Channel Length Achieving ON/OFF Ratio Exceeding 10^{11} , SS of 68 mV/dec, Normal-off Operation and High Positive Gate Bias Stability, *2023 IEEE Symposium on VLSI Technology and Circuits (VLSI Technology and Circuits)*, IEEE: 2023; pp 1-2.
- (11) Wang, C.; Kumar, A.; Han, K.; Sun, C.; Xu, H.; Zhang, J.; Kang, Y.; Kong, Q.; Zheng, Z.; Wang, Y.; Gong, X. Extremely scaled bottom gate a-IGZO transistors using a novel patterning technique achieving record high G_m of 479.5 $\mu\text{S}/\mu\text{m}$ (V_{DS} of 1V) and f_T of 18.3 GHz (V_{DS} of 3 V), *2022 IEEE Symposium on VLSI Technology and Circuits (VLSI Technology and Circuits)*, IEEE: 2022; pp 294-295.
- (12) Aabrar, K. A.; Kirtania, S. G.; Deng, S.; Choe, G.; Khan, A.; Yu, S.; Datta, S. In Improved Reliability and Enhanced Performance in BEOL Compatible W-doped In₂O₃ Dual-Gate Transistor, *2023 International Electron Devices Meeting (IEDM)*, IEEE: 2023; pp 1-4.
- (13) Ha, D.; Lee, Y.; Yoo, S.; Lee, W.; Cho, M.; Yoo, K.; Lee, S.; Lee, S.; Terai, M.; Lee, T. Exploring innovative IGZO-channel based DRAM cell architectures and key technologies for sub-10nm node, *2024 IEEE International Memory Workshop (IMW)*, IEEE: 2024; pp 1-4.
- (14) Zhao, W.; Zhu, S.; Li, Q.; Hu, Q.; Liu, H.; Tong, A.; Zeng, M.; Huang, R.; Wu, Y. First Demonstration of Double-Gate IGZO Transistors with Ideal Subthreshold Swing of 60 mV/dec at Room Temperature and 76 mV/dec at 380 K Over 5 Decades and g_m Exceeding 1 mS/ μm with Contact Length Scaling, *2024 IEEE International Electron Devices Meeting (IEDM)*, IEEE: 2024; pp 1-4.
- (15) Lee, C.-G.; Cobb, B.; Dodabalapur, A., Band transport and mobility edge in amorphous solution-processed zinc tin oxide thin-film transistors. *Applied Physics Letters* **2010**, 97 (20)
- (16) Liu, S.; Jana, K.; Toprasertpong, K.; Chen, J.; Liang, Z.; Jiang, Q.; Wahid, S.; Qin, S.; Chen, W.-C.; Pop, E., Design guidelines for oxide semiconductor gain cell memory on a logic platform. *IEEE Transactions on Electron Devices* **2024**.
- (17) Ye, H.; Gomez, J.; Chakraborty, W.; Spetalnick, S.; Dutta, S.; Ni, K.; Raychowdhury, A.; Datta, S. Double-gate W-doped amorphous indium oxide transistors for monolithic 3D capacitorless gain cell eDRAM, *2020 IEEE International Electron Devices Meeting (IEDM)*, IEEE: 2020; pp 28.3. 1-28.3. 4.
- (18) Belmonte, A.; Oh, H.; Subhechha, S.; Rassoul, N.; Hody, H.; Dekkers, H.; Delhougne, R.; Ricotti, L.; Banerjee, K.; Chasin, A. Tailoring IGZO-TFT architecture for capacitorless DRAM, demonstrating $> 10^3$ s retention, $> 10^{11}$ cycles endurance and L_g scalability down to 14nm, *2021 IEEE International Electron Devices Meeting (IEDM)*, IEEE: 2021; pp 10.6. 1-10.6. 4.
- (19) Liu, M.; Li, Z.; Lu, W.; Chen, K.; Niu, J.; Liao, F.; Wu, Z.; Lu, C.; zeng Li, W.; Geng, D. First Demonstration of Monolithic Three-Dimensional Integration of Ultra-High Density Hybrid IGZO/Si SRAM and IGZO 2T0C DRAM Achieving Record-Low Latency (< 10 ns), Record-Low Energy (< 10 fJ) of Data Transfer and Ultra-Long Data Retention (> 5000 s), *2024 IEEE Symposium on VLSI Technology and Circuits (VLSI Technology and Circuits)*, IEEE: 2024; pp 1-2.
- (20) Luo, Y.; Dutta, S.; Kaul, A.; Lim, S. K.; Bakir, M.; Datta, S.; Yu, S., A compute-in-memory hardware accelerator design with back-end-of-line (BEOL) transistor based reconfigurable interconnect. *IEEE Journal on Emerging and Selected Topics in Circuits and Systems* **2022**, 12 (2), 445-457.

- (21) Jang, Y.; Park, J.; Kang, J.; Lee, S.-Y., Amorphous InGaZnO (a-IGZO) synaptic transistor for neuromorphic computing. *ACS Applied Electronic Materials* **2022**, *4* (4), 1427-1448.
- (22) Tang, W.; Liu, J.; Sun, C.; Zheng, Z.; Liu, Y.; Yang, H.; Jiang, C.; Ni, K.; Gong, X.; Li, X., Low-power and scalable BEOL-compatible IGZO TFT eDRAM-based charge-domain computing. *IEEE Transactions on Circuits and Systems I: Regular Papers* **2023**, *70* (12), 5166-5179.
- (23) Liang, K.; Xu, X.; Zhou, Y.; Wang, X.; McCulley, C. M.; Wang, L.; Kulkarni, J.; Dodabalapur, A., Nanospikes electrodes and charge nanoribbons: A new design for nanoscale thin-film transistors. *Science advances* **2022**, *8* (4), eabm1154.
- (24) Liang, K.; Wang, X.; Zhou, Y.; Xu, X.; McCulley, C.; Wang, L.; Kulkarni, J.; Dodabalapur, A. In *Field-Emission Enhanced Contacts for Disordered Semiconductor based Thin-Film Transistors*, 2021 Device Research Conference (DRC), IEEE: 2021; pp 1-2.
- (25) Wang, L.; Fine, D.; Jung, T.; Basu, D.; von Seggern, H.; Dodabalapur, A., Pentacene field-effect transistors with sub-10-nm channel lengths. *Applied physics letters* **2004**, *85* (10), 1772-1774.
- (26) Das, M.; Sen, D.; Sakib, N. U.; Ravichandran, H.; Sun, Y.; Zhang, Z.; Ghosh, S.; Venkatram, P.; Subbulakshmi Radhakrishnan, S.; Sredenschek, A., High-performance p-type field-effect transistors using substitutional doping and thickness control of two-dimensional materials. *Nature Electronics* **2025**, *8* (1), 24-35.
- (27) Sun, Z.; Kim, S. Y.; Cai, J.; Shen, J.; Lan, H.-Y.; Tan, Y.; Wang, X.; Shen, C.; Wang, H.; Chen, Z., Low contact resistance on monolayer MoS₂ field-effect transistors achieved by CMOS-compatible metal contacts. *ACS nano* **2024**, *18* (33), 22444-22453.
- (28) Franklin, A. D.; Luisier, M.; Han, S.-J.; Tulevski, G.; Breslin, C. M.; Gignac, L.; Lundstrom, M. S.; Haensch, W., Sub-10 nm carbon nanotube transistor. *Nano letters* **2012**, *12* (2), 758-762.
- (29) Jariwala, D.; Sangwan, V. K.; Lauhon, L. J.; Marks, T. J.; Hersam, M. C., Emerging device applications for semiconducting two-dimensional transition metal dichalcogenides. *ACS nano* **2014**, *8* (2), 1102-1120.
- (30) Illarionov, Y. Y.; Knobloch, T.; Jech, M.; Lanza, M.; Akinwande, D.; Vexler, M. I.; Mueller, T.; Lemme, M. C.; Fiori, G.; Schwierz, F., Insulators for 2D nanoelectronics: the gap to bridge. *Nature communications* **2020**, *11* (1), 3385.
- (31) Wang, X.; Dodabalapur, A., Carrier Velocity in Amorphous Metal–Oxide–Semiconductor Transistors. *IEEE Transactions on Electron Devices* **2020**, *68* (1), 125-131.
- (32) Ko, J.-S.; Lee, S.; Bennett, R. K.; Schauble, K.; Jaikissoon, M.; Neilson, K.; Hoang, A. T.; Mannix, A. J.; Kim, K.; Saraswat, K. C., Sub-Nanometer Equivalent Oxide Thickness and Threshold Voltage Control Enabled by Silicon Seed Layer on Monolayer MoS₂ Transistors. *Nano Letters* **2025**.
- (33) Liang, K.; Zhou, Y.; McCulley, C. M.; Xu, X.; Dodabalapur, A., High-performance thin-film transistor device architecture for flexible and printed electronics. *Flexible and Printed Electronics* **2022**, *7* (3), 035015.

Supplementary information for

Enhancing gate control and mitigating short channel
effects in 20-50 nm channel length single-gate a-
IGZO Thin Film Transistors

Chankeun Yoon^{1,2} Yuchen Zhou,^{1,2} and Ananth Dodabalapur^{1,2,*}

¹ *Chandra Family Department of Electrical and Computer Engineering, The University of Texas
at Austin, Austin, Texas 78712, USA*

² *Microelectronics Research Center, The University of Texas at Austin, Austin, Texas 78758, USA*

Email: ananth.dodabalapur@engr.utexas.edu

Supporting Information 1

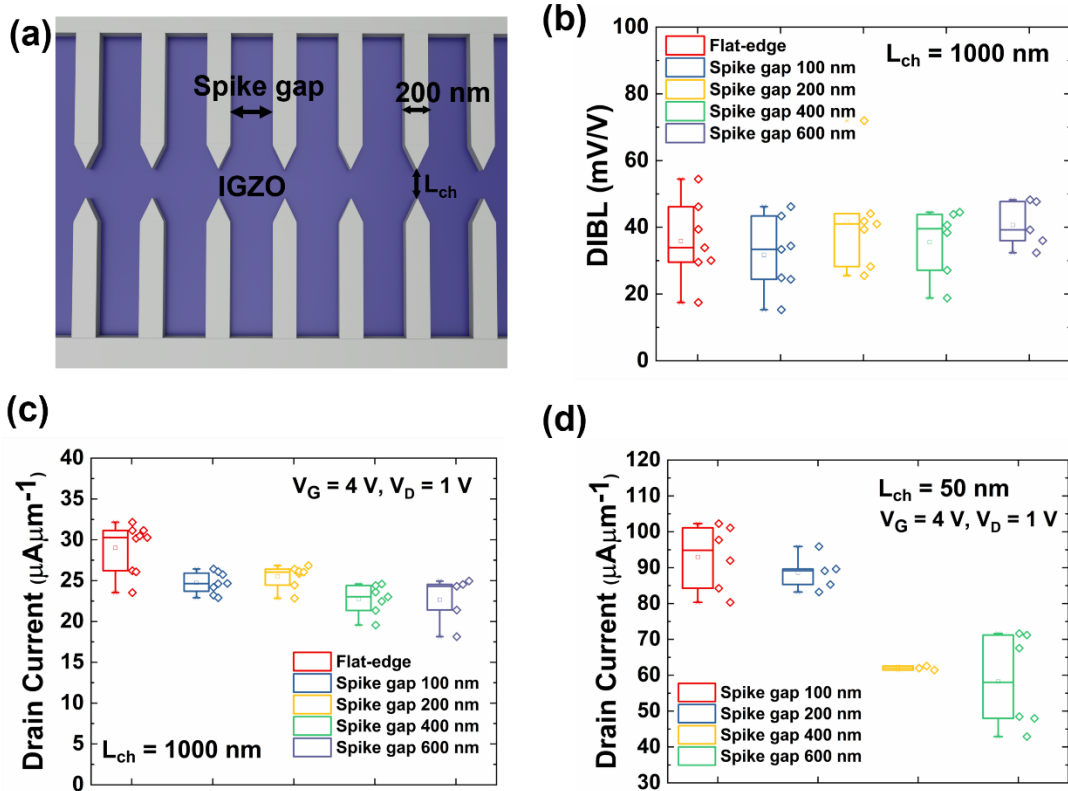


Figure S1. (a) Design of spike-shaped electrodes. (b) DIBL and (c) drain current comparison of 1000 nm L_{ch} devices with flat-edge electrode and spike electrode with various gaps between adjacent spike electrodes. (d) Drain current comparison of 50 nm L_{ch} spike devices with various gaps.

Figure S1a illustrates the schematic structure of the spike-shaped electrodes, where the gap between adjacent spike electrode is changed from 100 nm to 600 nm. In this comparison, the samples were not passivated with PMMA but were measured under vacuum conditions. **Figure S1b** and **S1c** shows the DIBL characteristics and I_{DS} of 1000 nm L_{ch} devices. Since L_{ch}/λ is large, all devices exhibit small DIBL values (< 100 mV/V) and the impact of gap variation is not significant. However, as the gap decreases from 600 nm to 100 nm, the I_{DS} increases, as shown in **Fig. S1c**. This trend becomes more pronounced at 50 nm L_{ch} , as shown in **Fig. S1d**. Based on these results, a 100 nm gap between spike electrodes is chosen for this study.

Supporting Information 2

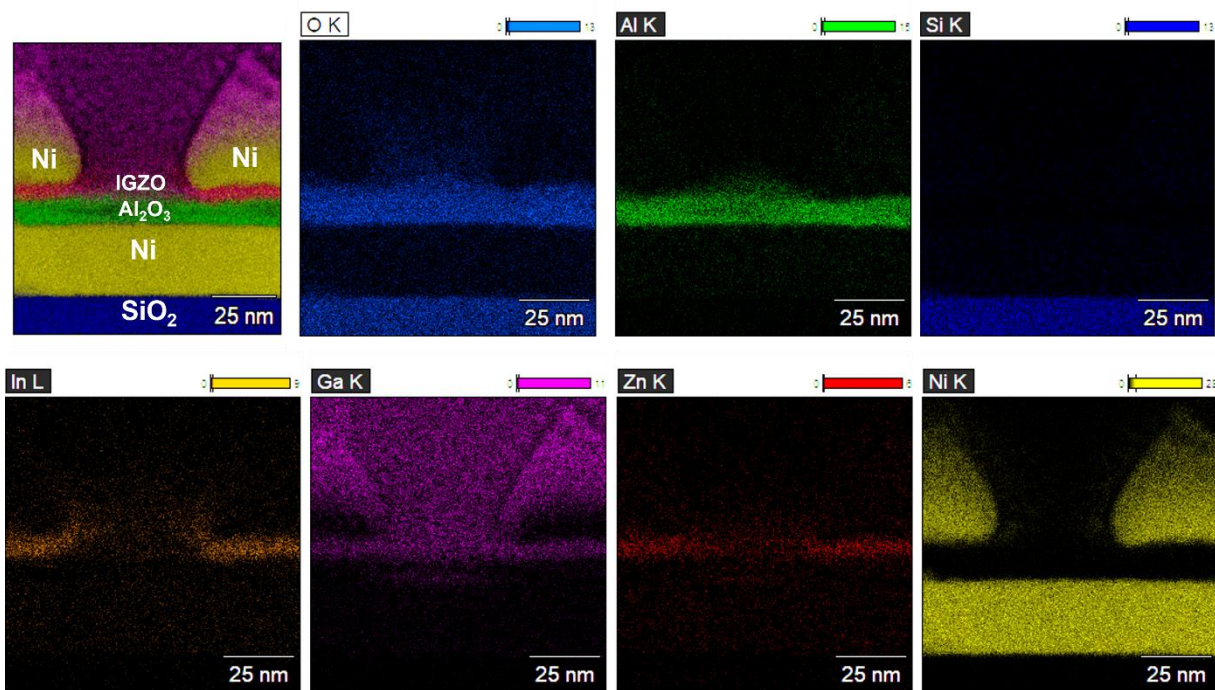


Figure S2. Cross-sectional Transmission Electron Microscopy (TEM) images with energy dispersive X-ray spectroscopy (EDS) elemental mapping of the 50 nm L_{ch} flat-edge device. Ga distribution is influenced during FIB cutting which used Ga ion for TEM sample preparation.

Supporting Information 3

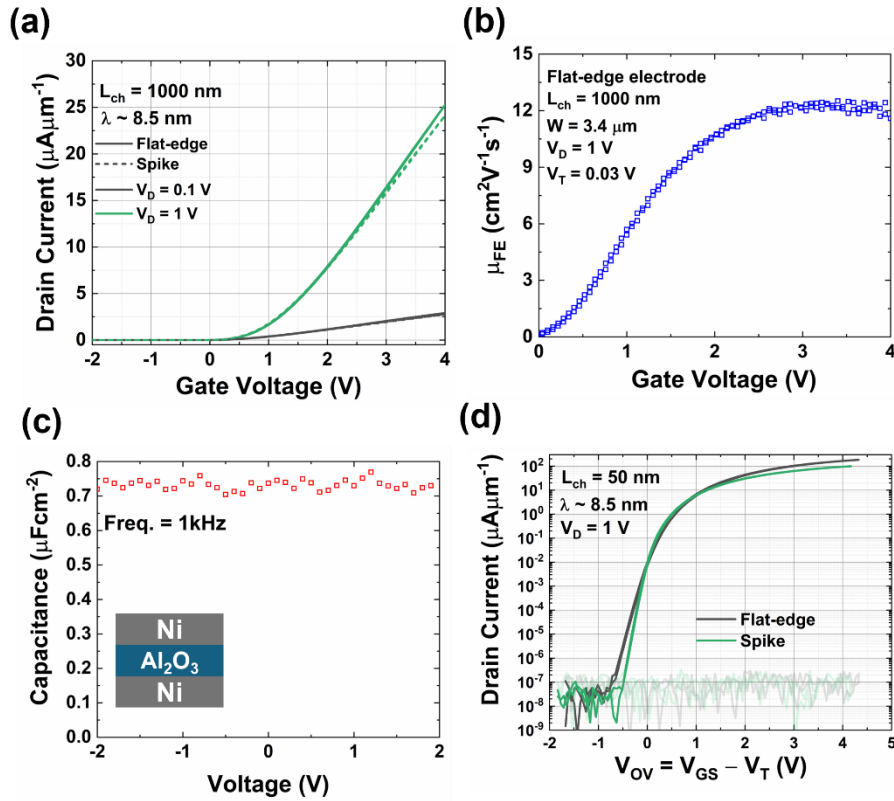


Figure S3. (a) I_D - V_G transfer characteristics of 1000 nm L_{ch} flat-edge and spike device, plotted in a linear scale. (b) Field effect mobility of 1000 nm L_{ch} flat-edge device. The calculated average mobility is $10 \text{ cm}^2\text{V}^{-1}\text{s}^{-1}$ at $V_G = 4$ V and $V_D = 1$ V. (c) Measured capacitance vs. voltage characteristics of Ni/Al₂O₃/Ni capacitor at 1 kHz. (d) I_D - V_{ov} characteristics of 50 nm L_{ch} flat-edge and spike device.

Figure S3a illustrates I_D - V_G of 1000 nm L_{ch} flat-edge and spike devices in linear scale showing comparable current. Field-effect mobility, μ_{FE} of 1000 nm L_{ch} flat-edge device is plotted in **Fig. S3b** ($\mu_{FE} = g_m L / (WC_{ox} V_D)$). **Fig. S3c** shows capacitance vs. voltage of 9 nm thick Al₂O₃ used in this study to calculate relative dielectric constant of Al₂O₃. Steeper turn-on behavior of 50 nm L_{ch} spike device is illustrated in **Fig. S3d**.

Supporting Information 4

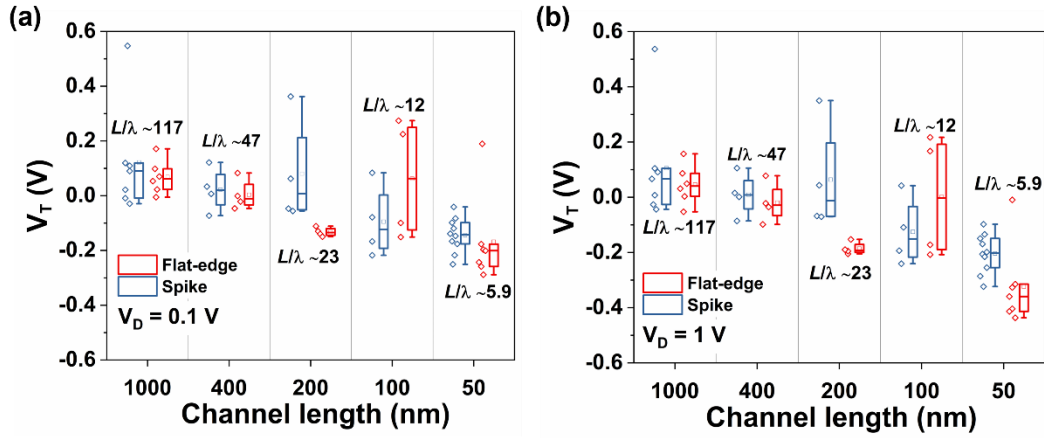


Figure S4. V_T comparison between spike and flat-edge devices at various L_{ch}

Supporting Information 5

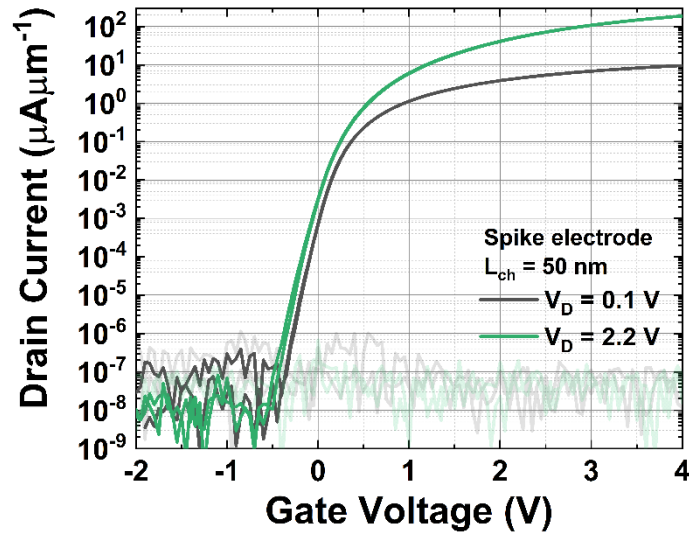


Figure S5. (a) I_D - V_G transfer characteristics of 50 nm L_{ch} spike device at $V_D = 0.1$ V and 2.2 V. SS remains low at 127 mV/dec under $V_D = 2.2$ V.

Supporting Information 6

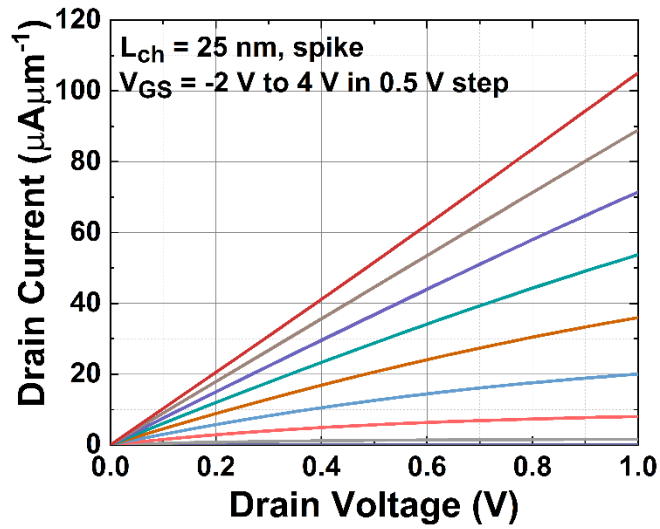


Figure S6. I_D - V_D output characteristics of 25 nm L_{ch} spike device.

Supporting Information 7

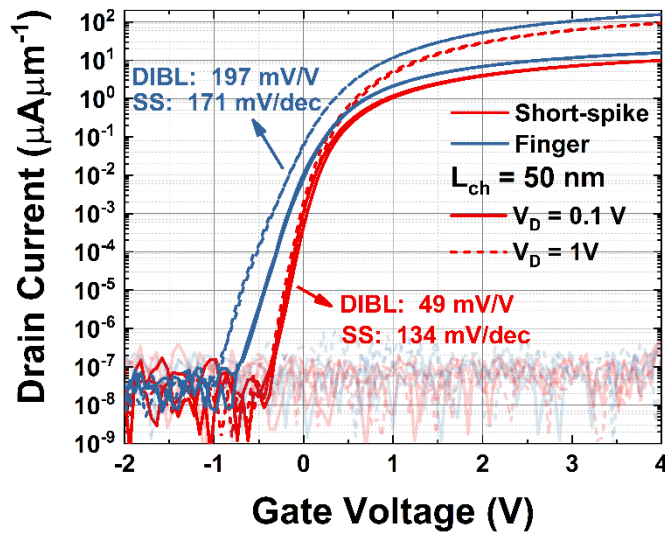


Figure S7. I_D - V_G transfer characteristics of 50 nm L_{ch} finger and short-spike device.